International Journal of Refrigeration 107 (2019) 275–287

Contents lists available at ScienceDirect

International Journal of Refrigeration

journal homepage: www.elsevier.com/locate/ijrefrig

Characterization and numerical simulation of liquid refrigerant R-134a flow emerging from a flooded evaporator tube bundle

William E. Asher*, Steven J. Eckels

Department of Mechanical and Nuclear Engineering, Kansas State University, Manhattan, KS, USA

ARTICLE INFO

Article history:
Received 1 March 2019
Revised 9 June 2019
Accepted 1 July 2019
Available online 5 July 2019

Keywords:
Numerical simulation
Droplets
Evaporator
Refrigerant
Tube bundle

ABSTRACT

The distribution of liquid droplets emerging from an evaporator tube bundle is characterized for refrigerant R-134a with a triangular tube arrangement with a pitch of 1.167. The purpose of this research was to improve understanding of the droplet ejection process to aid in design of evaporators typically used in larger chiller systems. A laser and camera system captured images of the evaporator headspace at varying conditions. Conventional shadowgraphy techniques were applied to recognize and match droplets for velocity calculations. The evaporator conditions varied with bundle mass fluxes of 20.3 and 40.7 kg $s^{-1}m^{-2}$, top-rows heat fluxes of 15.8 and 31.5 kWm^{-2}, and outlet saturation temperatures of 4.4 and 12.8 °C. Conditions ranged from flooded to dryout of the top rows. Droplet number, size distribution, velocity, and liquid volume fraction are presented in the headspace above the bundle. A method to numerically duplicate the droplet loading in the headspace using CFD with a Lagrangian discrete-phase model is also presented and verified, providing a powerful design tool. Liquid distribution in the headspace is found to be a strong function of all varied properties, particularly mass flux, liquid level, and saturation temperature.

Caractérisation et simulation numérique de l'écoulement du frigorigène R-134a à l'état liquide sortant du faisceau de tubes d'un évaporateur noyé

Mots-clés: Simulation numérique; Gouttelettes; Évaporateur; Frigorigène; Faisceau de tubes

1. Introduction

Control of liquid carryover in most larger refrigeration systems of shell-and-tube construction is a significant design issue. Achieving control requires an understanding of the mechanisms that create liquid droplets and methods of preventing migration of liquid droplets out of the evaporator. Two primary mechanisms assumed to play a role in the formation of droplets are shear and wave action. High vapor velocity causes shear in the bundle that entrains droplets into the flow. Depending on liquid distribution within the bundle, a liquid layer may exist above the bundle. The wave action of this layer may form droplets that entrain into the vapor flow. Aerodynamic forces, gravity, and droplet morphology are thought to control the migration of the liquid droplets once in the evaporator headspace. The refrigerant used, capacity of the chiller, and bundle geometry determine gas velocities within the bundle and headspace. These velocities are crucial in droplet carryover. With low-pressure refrigerant R-123, a vapor velocity of 15 m s^{-1} in the gaps between tubes can be expected, capable of lifting droplets of millimeter scale. For the same conditions, a refrigerant such as R-134a will only have a velocity of 2 m s^{-1}, reducing expected droplets to sub-millimeter size. Vapor in the headspace slows as the cross-sectional area increases and larger droplets fall back onto the bundle. Evaporation of liquid in the headspace, dictated by the thermodynamic conditions of the flow, can also affect droplet morphology. Slightly superheated vapor with saturated liquid droplets in the flow field can occur, wherein droplets may evaporate as they flow through the headspace.

* Corresponding author.
E-mail addresses: asherw@ksu.edu, asherwe@ornl.gov (W.E. Asher), eckels@ksu.edu (S.J. Eckels).

https://doi.org/10.1016/j.ijrefrig.2019.07.001

Nomenclature

$A_{tube,o}$	outer surface area per tube
$c_{p,\,w}$	water specific heat
d	droplet diameter
$\bar{D}_i$	volume-averaged droplet diameter per bin
$\bar{d}$	mean droplet diameter of Rosin-Rammler curve
d_{max}	mean droplet diameter of Rosin-Rammler curve
d_{min}	mean droplet diameter of Rosin-Rammler curve
DOF	depth of focus
e	Euler's number
H	height of bin for liquid volume fraction
$\dot{m}_T$	total mass liquid- flow rate
$\dot{m}_v$	mass liquid-flow rate per binned velocity, all diameters
$\dot{m}_{v,d}$	mass liquid-flow rate per binned velocity and per binned diameter
$\dot{m}_w$	water mass flow rate per tube
n	shape parameter of Rosin-Rammler curve
n_i	number of droplets per binned height
N	number of bins for discretizing droplet diameter
P_{in}	tube water inlet pressure
P_{out}	tube water outlet pressure
ϕ_i	liquid volume fraction per binned height
q''_{tube}	heat flux per tube
ρ_w	water density
T_{in}	tube water inlet temperature
T_{out}	tube water outlet temperature
U_ϕ	liquid volume fraction uncertainty
$V_{l,\,total,\,i}$	total liquid volume per bin
W	width of bin for liquid volume fraction
Y_d	cumulative mass fraction based on droplet diameter
Y_v	cumulative mass fraction based on droplet velocity
$high$	denotes high bound of bin for injection calculation
low	denotes low bound of bin for injection calculation

Droplets may impact upon the walls of the headspace and objects such as distribution plates placed in the path of the flow. Finally, droplets can coalesce into larger droplets, exceeding the carrying capacity of the vapor and falling back to the bundle. Experimental data would allow the means to understand the relative impact of aerodynamic forces, thermodynamics (heat transfer), and wave breakup, enabling better headspace design.

The goal of the research project was to experimentally record the liquid droplets that emerge from the top of a tube bundle under typical operating conditions. Data generated includes droplet position, velocity, and size within the headspace of the bundle for varied operating conditions. The experimental data should provide insight into the physics that control movement and liquid formation within the headspace, providing critical validation data for those doing numerical simulation.

The paper recalls the unique experimental facility developed to measure droplet size, velocity, and count in the headspace of an R-134a enhanced-tube bundle. Results of the experimental study are discussed and analyzed. A method for numerically simulating the liquid distribution in the headspace is described and a comparison is made with experimental results. Finally, a discussion of both the experimental and numerical results is presented.

2. Literature review

The large experimental facilities required for research lead to shell-side evaporator performance receiving significantly less experimentation in the past than other evaporation arrangements. The study of local heat transfer and pressure drop as refrigerant flows through enhanced-tube bundles primarily using 19.05 mm (0.75 inch) tubes with a standard pitch of 1.167 is one important class of experiments with refrigerant shell-side evaporators. Van Rooyen and Thome (2014) and Van Rooyen and Thome (2013) studied R-134a and R-236fa in enhanced-tube bundles, documenting local heat transfer coefficients and pressure drop in the bundle. Gorgy and Eckels (2013) documented similar data for R-123 and R-134a on enhanced-tube bundles of standard pitch while with the same facility results for variable-pitch bundles were given for R-134a by Gorgy and Eckels (2016), and for R-123 by Gorgy and Eckels (2019). Robinson and Thome (2004) studied R-134a, R-410A, and R-507A in a similar bundle of standard pitch. All four heat-transfer studies had saturation temperatures of 4 and 15 °C, mass fluxes from 4 to 55 kg $s^{-1}m^{-2}$, and heat fluxes from 15 to 70 kW m^{-1}. Ribatski et al. (2008) investigated R-123 nucleate boiling on arrays of horizontal tubes with various pitches and heat fluxes from 0.5 to 40 kW m^{-2}, obtaining a correlation for heat-transfer coefficients. In none of these experiments was the headspace observed.

Flow-pattern studies within the bundle represent another class of experiments done on this standard rectangular bundle. van Rooyen et al. (2012) used a clear dummy tube with a digital high-speed video camera and a laser light/photodiode, as well as pressure-drop measurements, to predict internal flow patterns. Schlup and Eckels (2017) also report flow patterns in an enhanced-tube bundle by using a borescope and complementing experimental data with numerical analysis. Kanizawa and Ribatski (2016) studied vertical air-water flow across a tube bundle, using both pressure drop and capacitive sensors to quantify void fractions and flow patterns within the bundle. Development of flow-pattern maps from flow-visulizaiton data has been attempted in a number of studies (Cheng et al., 2008; Grant and Chisholm, 1979; Kondo and Nakajima, 1980; Ulbrich and Mewes, 1994).

The current study used a shadowgraphy technique to characterize droplets. With this method, a camera captures images of objects backlit by a light source, with the objects being delineated from their transparent medium by differences in refraction and opacity. Specifically, the objects are illuminated by the light source, and the area that the camera sees consists of a bright background with dark areas corresponding to the objects' boundaries. For this work, a dual-pulse Nd-Yag laser was the light source and a 4-megapixel camera was used. Of note, the equipment used in this work can also be used for particle image velocimetry (PIV) applications such as in Li et al. (2018). In Dai et al. (1998), both a single- and double-pulsed laser system were coupled with a film camera to capture droplet formation from turbulent liquid wall jets. Hay et al. (1998) incorporated use of a CCD sensor instead of film to speed processing in order to verify characteristics of two-phase annular flow in a vertical pipe. For Patruno et al. (2010) shadowgraphy was incorporated by use of a continuous white light source coupled with a high-speed digital camera to capture data on liquid entrainment from a wetted wire in high-gas-flow-rate cross flow. To apply shadowgraphy to characterize diesel injector spray, Blaisot and Yon (2005) used nanosecond flash flamps with a CCD camera with microscope optics, as well as described a method to account for out-of-focus droplets. Both Kashdan et al. (2003) and Kashdan et al. (2004) described development and use of an analysis technique to improve accounting of out-of-focus droplets and use of an infrared diode laser, coupled with a CCD camera, to compare results with those of phase-Doppler anemometry for small fuel droplets produced by a pressure-swirl atomizer. The methods chosen for this work most closely follow the methods of Hay et al. (1998).

A final class of research in this field involves numerical simulation of two-phase pool boiling. Ahmadpour et al. (2018) used a Eulerian–Eulerian approach with a two-dimensional model to

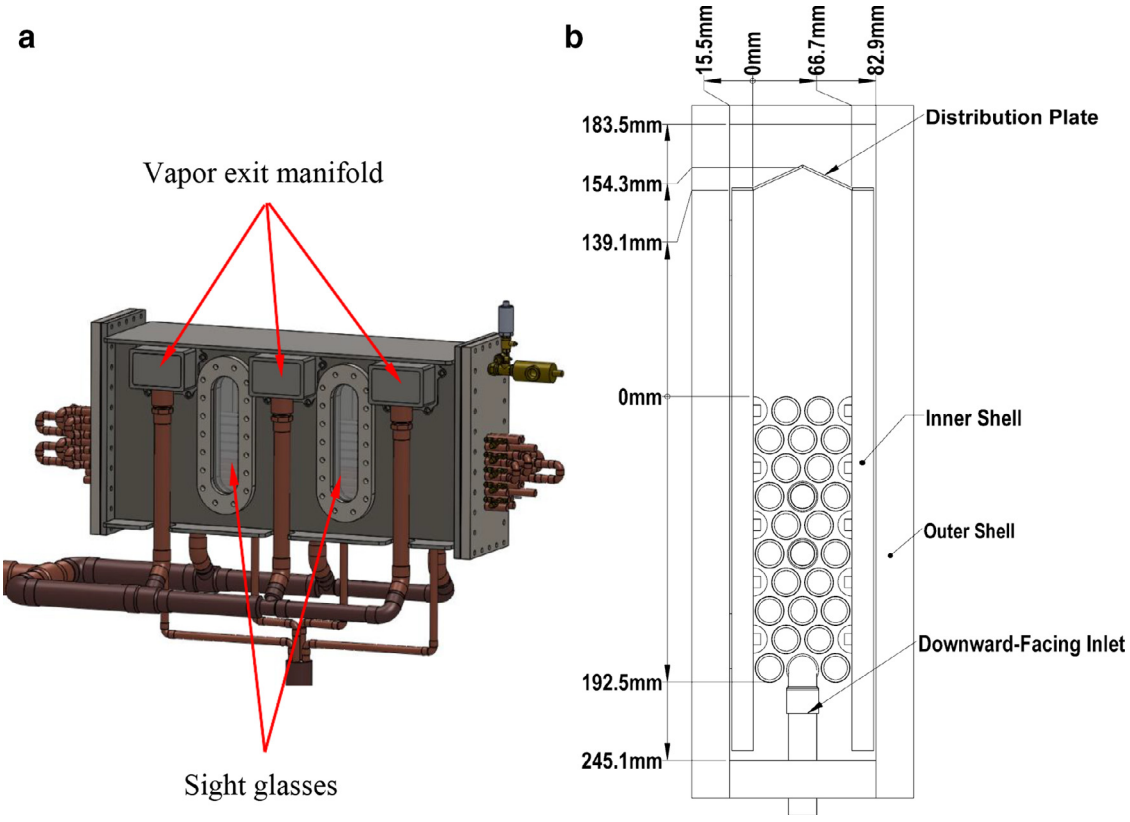

Fig. 1. Test section (a) model, (b) cross-section.

predict volume fraction within a bundle for a variety of refrigerants at a variety of conditions, achieving good agreement with the experimental results of Gupta (2005), Jung et al. (2003), and Kang (2016). Ahmadpour was inspired by the work of Minocha et al. (2016), which again used a Eulerian–Eulerian approach, albeit with a three-dimensional volume-of-fluid model. However, all these numerical simulations have been within the bundle, with no attention paid to the headspace. To date, no numerical simulations have been found modeling the headspace of evaporator bundles beyond this present work.

Table 1
Measurement uncertainties.

Variable	Uncertainty	Notes
Temperature, T	+0.1 C	Thermistors
Pressure, P	+0.15% full scale	Strain gauge transducers
Flow, $\dot{m}$	+0.1% reading	Coriolis type
Depth of Focus, DOF	+0.5 mm+0.2 mm	50-mm lens,100-mm lens
Droplet diameter, D	+21 μm+9 μm	50-mm lens100-mm lens
Image pair timing	10 ns	Impacts measured droplet velocity
Droplet Count	+10% value	

3. Facility description and image analysis

The minutiae of the test facility are described in Asher and Eckels (2018b), but a brief description is given. The key part of the test facility is the flooded evaporator test section with large sight glasses to allow observation of the headspace. The test section holds 20 enhanced tubes in a triangular arrangement. Liquid or two-phase refrigerant enters at the bottom of the test section, flows around the outside of the tubes, and exits the test section into a manifold as either vapor or a two-phase mixture. Depending on the desired conditions, water enters between 4.4 and 15 °C hotter than the refrigerant saturation temperature and flows through the tubes, providing the energy for evaporation of the refrigerant, and then leaves between 1 and 3 °C hotter than the refrigerant. A model of the test section is shown in Fig. 1(a), while the cross-sectional dimensions are shown in Fig. 1(b). The headspace is 66.7 mm wide and extends between 139.1 mm and 154.3 mm above the tubes. The distribution plate is 1.52 mm thick, extends the full length of the bundle, and contains 50 holes with a diameter of 8.13 mm. The holes alternate between 11.5 mm and 25 mm away from the peak and are uniformly spaced axially a distance of 38.46 mm. Note that axial denotes along the long dimension of the bundle, or rather, in and out of the page in Fig. 1(b).

Described in detail in Asher and Eckels (2018b), the shadowgraphy system consists of a camera and back-lighting laser across the bundle from each other. The laser releases a dual-pulses synchronized with the camera to capture a series of 100 image pairs. The time between images in a pair varies from 300 to 1800 μs based on expected droplet velocity due to flow conditions, and image pairs are captured at a rate of 7.25 Hz. An example of one image is shown in Fig. 2(a). The laser pulse passes through a motorized variable attenuator to control laser intensity and a 50° holographic diffuser to equalize intensity across the viewing area. These images were then processed to the form seen in Fig. 2(b) and analyzed using commercial software to generate the droplet data used for this research. Provisions in the software allow for masking the region near the tubes as well as filtering out droplets based on circularity and size, though some droplets can be combined erroneously by the droplet recognition algorithm.

Uncertainties for physical and optical measurements are given in Table 1. Temperature, pressure, flow, and timing uncertainties are based on the manufacturer's specifications. Uncertainties for the remaining optical measurements are based on observation and

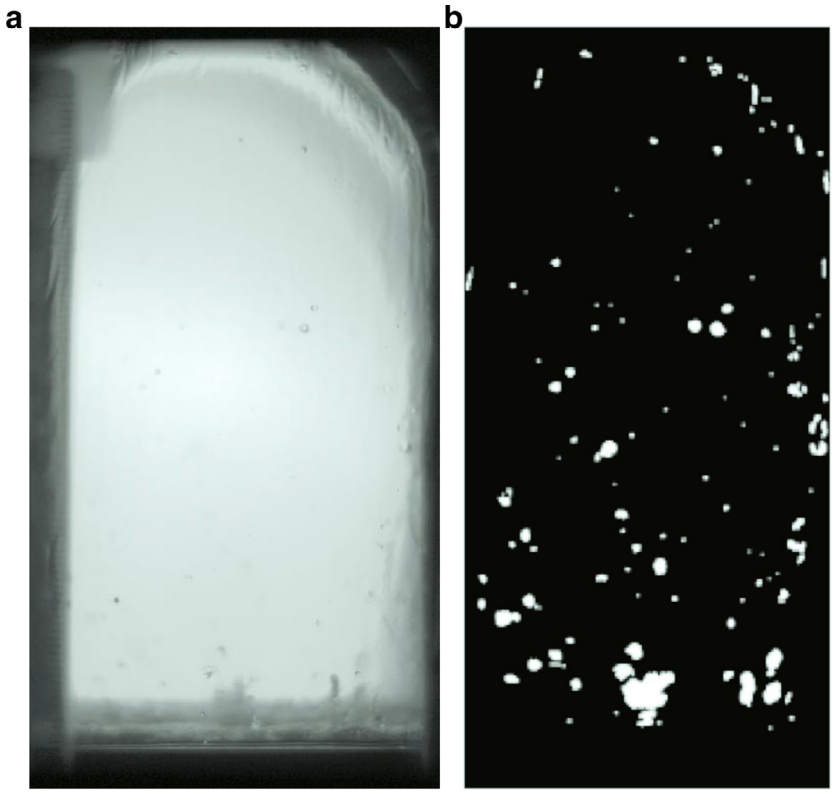

Fig. 2. Example images- (a) as taken, (b) processed.

Table 2
Experimental test conditions.

Saturation temperature °C	Mass fluxkg s^{-1} m^{-2}	Top-rows heat fluxkW m^{-2}
4.4	20.3	15.7
4.4	20.3	23.3
4.4	40.7	15.7
4.4	40.7	31.5
12.8	20.3	15.7
12.8	20.3	22.7
12.8	40.7	15.7
12.8	40.7	31.5

calibration. A propagation of uncertainties further resulted in ±1% for mass flux and ±4.1% for heat flux.

4. Experimental results

The test matrix of experimental conditions in Table 2 shows the variation of saturation temperature, mass flux, and top-rows heat flux. Note that the top-rows heat flux is the mean heat flux of the top two rows of tubes, meaning the mean of the top five tubes shown in Fig. 1(b). The heat flux is determined by Eq. (1), calculating the rate of energy change across each tube and dividing by the tube area. Mass flux is determined by the refrigerant mass flow rate divided by the minimum area between the top tube row.

$$q''_{tube} = \dot{m}_w \left[c_{p,w}(T_{in} - T_{out}) + \frac{(P_{in} - P_{out})}{\rho_w} \right] / A_{tube,\,o} \quad (1)$$

The liquid level in the bundle is an additional important factor. The liquid level can be thought of as the liquid that sits atop the bundle through which vapor must pass. This liquid level is directly tied to the top-rows heat flux. In an actual system, the liquid level would depend on the refrigerant charge, evaporator design, and headspace design. The liquid level in the test system was controlled by removal and addition of refrigerant from the system. Runs of data for each setpoint in Table 2 were obtained with a high liquid level, low liquid level, and ideal level. The high liquid level was roughly defined as a visible pool of liquid flooding approximately 25 mm above the tubes. The low liquid level was a dryout condition defined by approximately a halving of the heat-transfer coefficient in the top rows. The ideal liquid level was defined as the lowest liquid level possible before dryout occurred on the tubes. This would represent a minimum refrigerant charge in the system for optimum performance.

Baseline data for R-134A at 12.8 °C with a mass flux of 20.3 kg s^{-1} m^{-2} and an upper-rows heat flux of 15.7 kW m^{-2} with the 50-mm lens is shown in Fig. 3. Each subfigure represents an average of 100 images (first image taken per image pair). Subfigure (a) shows total counts of matched and unmatched droplets. Subfigure (b) shows droplet counts per each 5 mm of bin height above the tube and indicates no carryover of droplets that have been imaged, with droplet counts trailing to zero by 65 mm above the tubes. Subfigure (c) shows the size distribution of droplets, with droplets strongly tending toward smaller diameters. Plots of velocity in subfigure (d) only represent droplets that were matched between image pairs. The roughly symmetrical distribution about 0 m s^{-1} indicates that droplets that rise largely will fall back down, again showing no carryover out of the headspace, at least with the droplets capable of being imaged. As discussed in Asher and Eckels (2018b), the data shown has depths of focus for the 50-mm lens of 3.52 mm and 1.37 mm for the 100-mm lens. This gives a relative sense of the vapor space where these droplets are counted.

For comparison of results between different test conditions and methods, the liquid volume fraction developed in Asher and Eckels (2018b) is used as it combines both height and diameter into one chart. In short, liquid fraction is found by calculating the total liquid droplet volume per binned height and dividing by both the binned volume and the total number

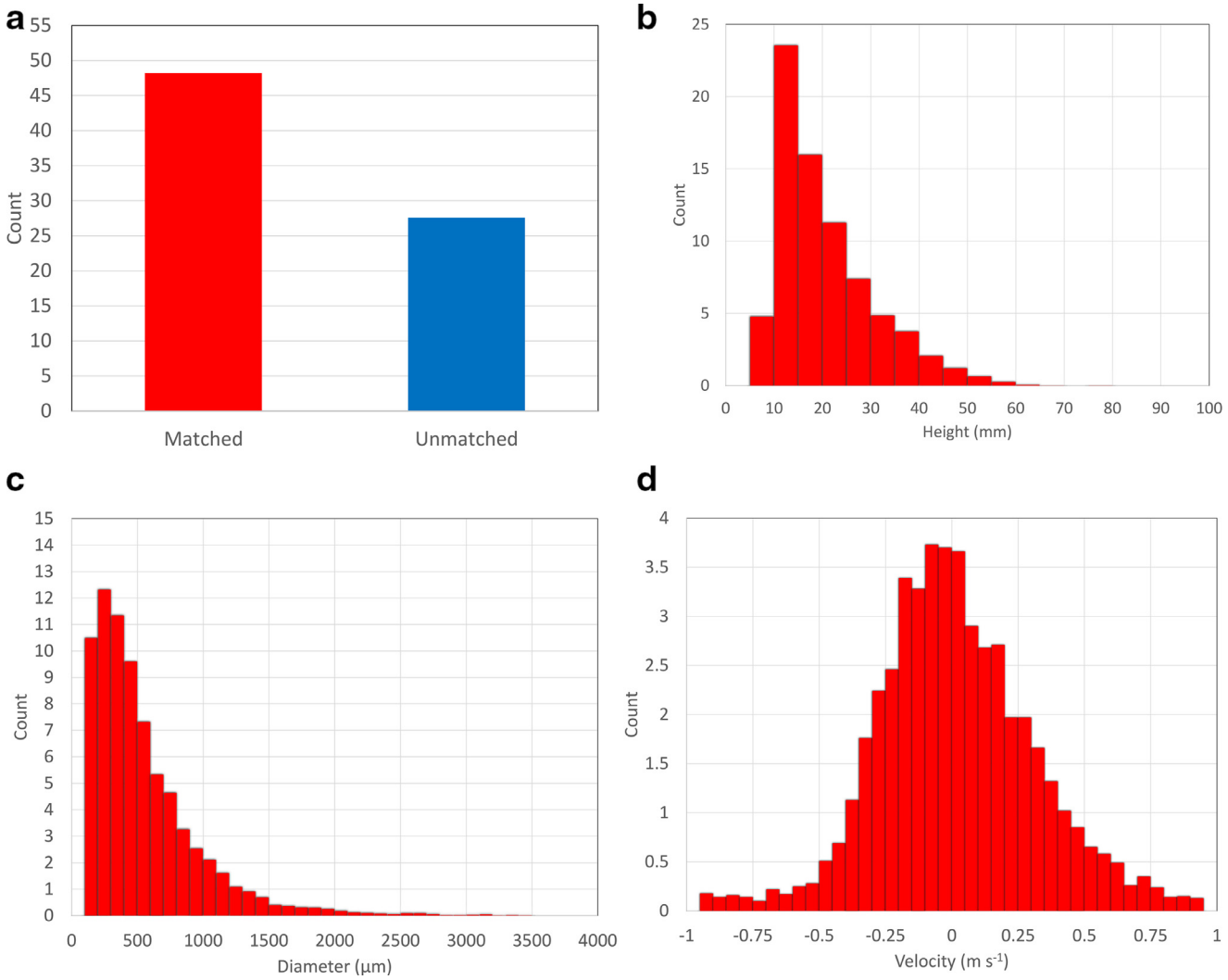

Fig. 3. Data summary for 12.8 °C at 20.3 kg s^{-1} m^{-2} with 15.7 kW m^{-2} top-rows heat flux with 50-mm lens, showing (a) total counts, (b) counts versus height, (c) counts versus size, and (d) velocity distribution for ideal liquid-level case; all charts are averages of 100 images.

of images. While in actuality these volumes are calculated on a by-droplet basis and account for droplets that span more than bin, an approximation of this process can be given by Eq. (2), with the definition of $\bar{D}_i$, the volume-averaged droplet diameter per bin, being given by Eq. (3).

$$\phi_i = n_i \frac{\pi \bar{D}_i^3}{6H \cdot W \cdot DOF} \tag{2}$$

$$\bar{D}_i = \sqrt[3]{\frac{6V_{l,total,i}}{n_i}} \tag{3}$$

Here, the liquid volume fraction is ϕ_i, the number of droplets is n_i and the liquid volume is $V_{l,\,total,\,i}$, all per binned height. The height of the bin is H (5 mm), width is W (35 mm), and depth of focus is DOF (3.52 or 1.37 mm for 50 mm and 100 mm lens, respectively.

The resultant uncertainty liquid volume fraction per bin is then found from Eq. (4). Uncertainties range up to a maximum of ±44% for one bin of one test, though the median uncertainty is ±20%.

$$U_\phi = \sqrt{\left(\frac{\partial \phi}{\partial n} U_n\right)^2 + \left(\frac{\partial \phi}{\partial \bar{D}} U_{\bar{D}}\right)^2 + \left(\frac{\partial \phi}{\partial DOF} U_{DOF}\right)^2} \tag{4}$$

Fig. 4 shows the effects of variation of mass flux, liquid level, saturation temperature, and heat flux on the liquid volume fraction above the headspace. It also illustrates differences between the base 50-mm lens and the higher-magnification 100-mm lens. Baseline denotes the same set of data illustrated in Fig. 3.

The baseline case in Fig. 4 shows a liquid mass fraction of 0.007 at 17.5 mm above the tubes that decreases exponentially to a liquid mass fraction of 0 at about 70 mm above the tubes. For all cases, minimum height of the liquid volume fraction shown was limited by either field of view, such as with the 100-mm lens, or due to the density of droplets or liquid waves preventing the imaging of droplets, as seen with the flooded and high-mass-flux variations.

The largest variation seen in Fig. 4 is due to the evaporator being flooded. Flooded, again, refers to having conditions of approximately 25 mm of visible liquid pooled atop the tube bundle. Typically, when observing droplet count vs. height as shown in Fig. 3(b), a simple shift upwards in height by approximately 25 mm is seen for the flooded liquid level compared with the baseline. However, observing the liquid volume fraction of Fig. 4, a shift of approximately 35 to 40 mm occurs and the flooded case has a maximum liquid volume fraction of 0.0367 at 27.5 mm, compared with 0.007 for the baseline case at 17.5 mm, which occurs for the flooded case at 52.5 mm. This observation tells us that larger

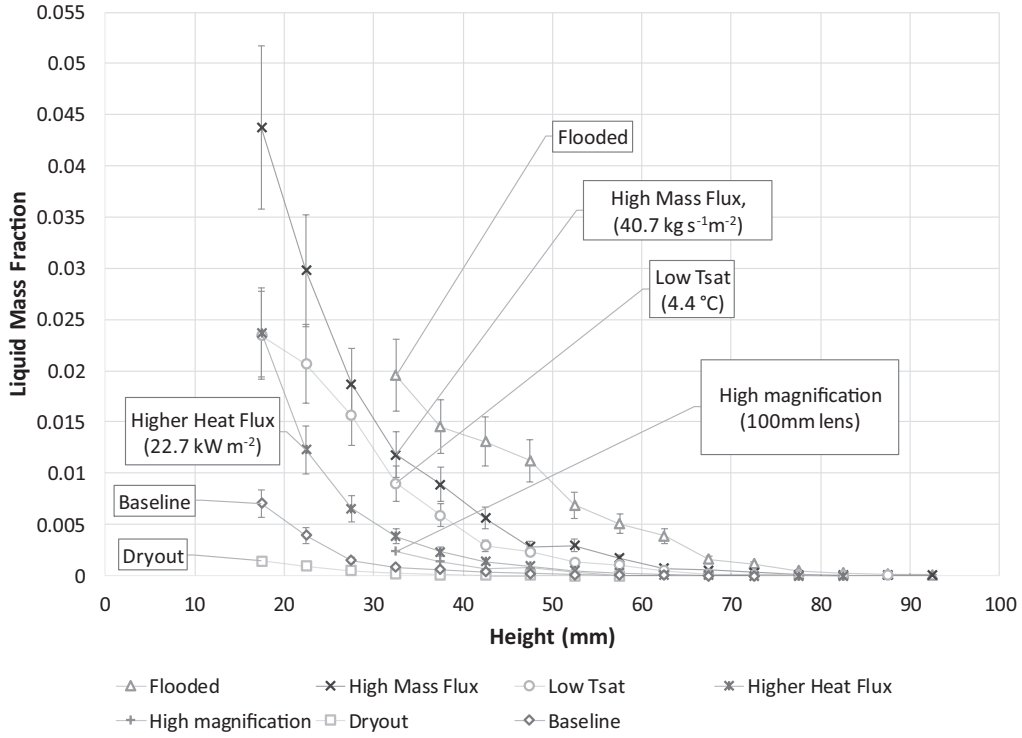

Fig. 4. Effects on liquid volume fraction of deviating from baseline case of 12.8 °C at 20.3 kg s^{-1} m^{-2} with 15.7 kW m^{-2} and 50-mm lens.

Table 3
v_{max} as a function of mass flux and saturation temperature.

Mass flux (kg s^{-1} m^{-2})	Saturation temperature (°C)	v_{max} (m s^{-1})
20.3	12.8	1.00
20.3	4.4	1.30
40.7	12.8	1.97
40.7	4.4	2.61

droplets must be generated in the flooded case because the shift in volume fraction can't be explained by droplet counts alone.

The high-mass-flux variation shows the next-largest deviation from the baseline. At the lowest common height of 17.5 mm, the liquid volume fraction for the high-mass-flux curve is 0.044, approximately six times higher than the baseline at 0.007. The higher amount of liquid extends out nearly to the top of the headspace, reaching a liquid volume fraction of zero at 92.5 mm. The larger amount of liquid throughout the headspace is expected, as doubling of the mass flux causes a doubling of vapor velocities in the bundle, both between the tubes and in the headspace. The higher the velocity, the greater the diameter of droplets the vapor can carry and the greater the number of droplets generated by the flow.

The variation seen with changing saturation temperatures is explained by the velocities involved. Observing Table 3, maximum velocity expected between the tubes for the baseline case of 1.00 m s^{-1} is increased to 1.30 m s^{-1} by decreasing the temperature to 4.4 °C. As with increasing the mass flux, increased velocity both in the headspace and between the tubes increases the size of droplets the vapor is able to carry. Indeed, it is not until approximately 35 mm that the lower saturation temperature curve has decreased to match the baseline at a liquid volume fraction of 0.007.

With the higher-heat-flux comparison, it is important to note the heat flux of 22.7 kW m^{-2} as shown in Table 2 is not at the originally specified 31.5 kW m^{-2}. At the baseline mass flux of 20.3 kg $s^{-1}m^{-2}$ and saturation temperature of 12.8 °C, a top-rows heat flux of 22.7 kW m^{-2} was the highest mass flux that could be achieved with this system. Still, significant differences are seen in the liquid volume fraction of Fig. 4 from the baseline. A maximum value of 0.024 is seen compared with 0.007 for the baseline, both at 17.5 mm above the tube. It is not until an additional 7 to 10 mm above the tubes that the higher-heat-flux curve meets the baseline maximum liquid volume fraction. It is proposed these increases from the baseline are due to requiring more liquid at the tubes to maintain a higher heat flux, increasing the possibility of liquid being entrained in the flow. The effect is less pronounced when comparing heat fluxes at the higher mass flux (not shown), as the increased velocities both likely increase the chance of liquid evaporating on the tubes, and the higher velocities likely overbear the effect of increased liquid at the walls.

Dryout conditions in Fig. 4 show a significant decrease from the baseline in the liquid volume fraction. Much less liquid is present at the tube walls, with the majority having evaporated before entering the headspace from the tube bundle. A heat-transfer coefficient ratio of 0.5 to 0.6 between the top two tube rows was the criteria for dryout and occurs roughly at a halving of the overall heat flux in the top two rows. The liquid volume fraction for the dryout case is approximately four to six times less than the baseline for most of its curve, though both the baseline and dryout curves go to a value of zero between 60 and 70 mm above the tubes.

Finally, a comparison is shown between the 100-mm lens and the 50-mm lens of the baseline. The 50-mm lens was capable of resolving droplets of approximately 128 µm, whereas the 100-mm lens was capable of resolving droplets down to 57 µm, albeit with a restricted field of view from 30 to 75 mm above the tubes. In addition, the 100-mm lens was capable of making out finer distinctions in larger droplets. The apparent increase in the liquid volume fraction of approximately three times that of the baseline may be explained by the ability to resolve those droplets below 128 µm as well as the ability to more accurately resolve larger droplets.

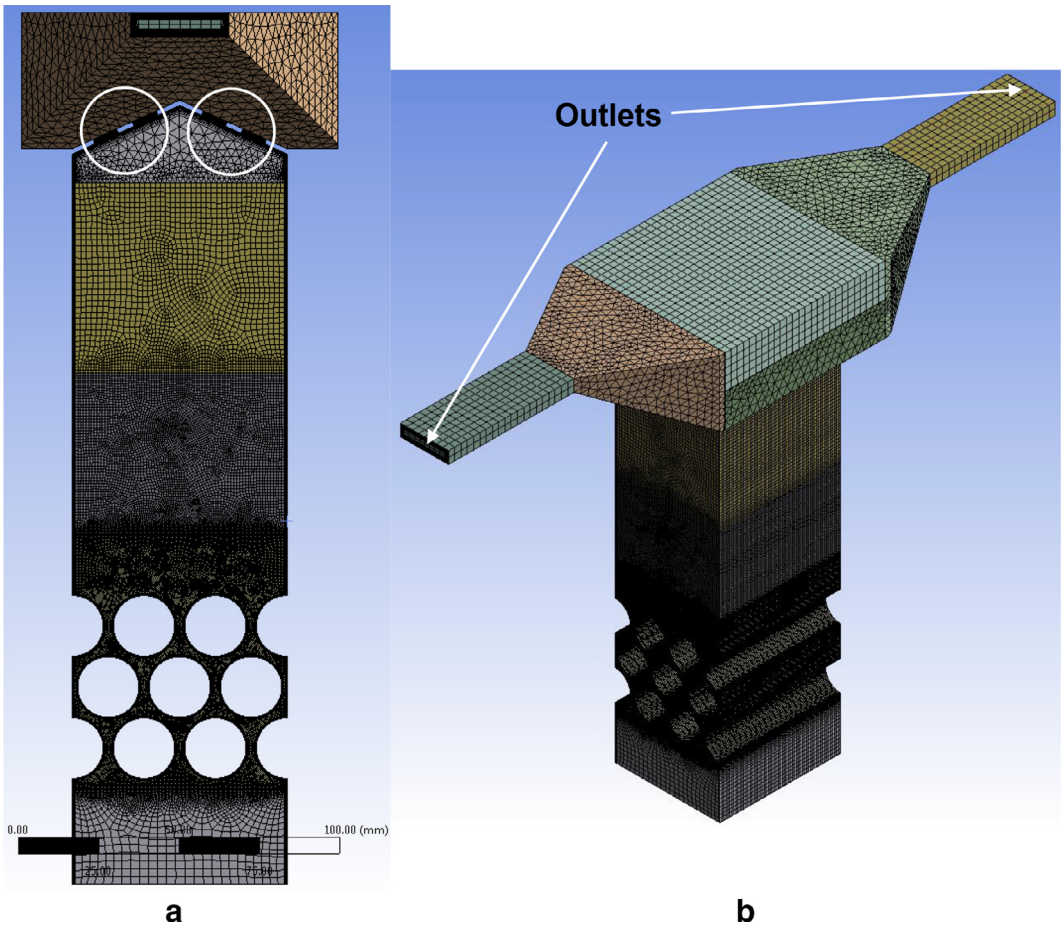

Fig. 5. Meshed simulation volume – (a) axial view, (b) isometric view.

5. Numerical simulation

To complement the experimental results, a section of the bundle was numerically simulated with the aim of finding a numerical method of replicating liquid distribution in the headspace. The flow field was first established by simulating pure vapor. Droplets were then injected as inert particles with Lagrangian particle physics, not influencing the vapor flow. The following sections describe the setup and highlight insights gained from the pure-vapor simulation and then when droplets were simulated.

5.1. Vapor simulation setup

The vapor simulation was bounded by the test-section walls and restricted to an axial length of 76.9 mm. Features include three rows of tubes and half tubes as well as two pairs of distribution-plate holes (circled) as shown in Fig. 5(a). The space above the distribution plate carried the same dimensions as the real test section, but flow was directed axially and narrowed to remove reverse flow at the outlets. The axial flow also simulates conditions that exist above the viewing windows in the physical test section as there, the outlet manifold carries refrigerant away from the test section on either side of the window.

Views of the meshed volume are shown in Fig. 5. An inlet region below the tubes with a height of 30 mm was created and set to have a coarse mesh size of 3 mm. The region containing the tubes had a nominal mesh size of 0.5 mm, extending to 20 mm above the top tubes. A size of 0.5 mm was chosen to achieve at least five elements between the opposing inflation layers between tubes once mesh inflation was applied. The region from 20 mm to 70 mm above the top tubes had a mesh size of 1 mm. The region from 70 mm to 130 mm above the top tubes had a mesh size of 2 mm. The preceding meshes were all swept hexehedral meshes, having 40 elements across the axial length of the simulation space. The region following extended to the distribution plate and contained a free mesh consisting of tetrahedral and hexahedral elements of 2-mm size, with a region of influence centered at each distribution- plate hole of a diameter of 5 mm and a mesh size of 0.5 mm. The region above the plates consisted of a mixture of swept and free meshes of sizes from 2 to 4 mm. An inflation of 15 layers and thickness of 0.8 mm was applied to all wall surfaces in the swept regions below the distribution plate while a smooth inflation of 15 layers was applied to all other walls. The resultant mesh contained 3.29e6 elements and 3.66e7 nodes. A grid independence study was performed by progressively doubling the size of elements as previously described, up to a maximum size of 4 mm. The static pressure drop from inlet to outlet was sampled, resulting in Table 4 below, converging on a pressure drop of 1388 Pa with the two finer meshes.

Table 4
Pressure drop from inlet to outlet as function of mesh refinement.

Number of elements ($\times 10^5$)	Pressure drop (Pa)
4.8	1263
7.3	1352
15.0	1388
32.9	1388

A translational periodic boundary condition was applied to the axial surfaces below the distribution plate to simulate a long test

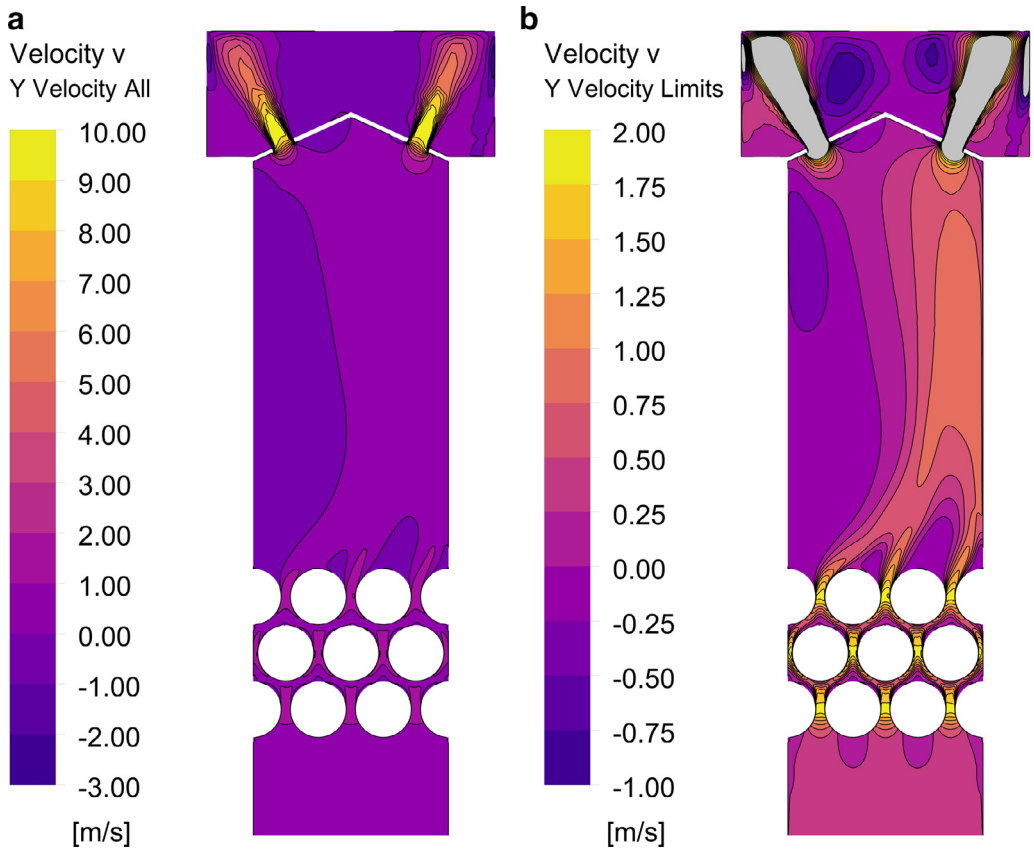

Fig. 6. Vertical velocity in x-y plane for 40.7 kg s^{-1} m^{-2} (a) global range (b) constrained range for detail.

section. For two separate simulations, mass inflow boundary conditions of 0.0149 and 0.0298 kg s^{-1} were applied to the bottom inlet, corresponding to mass fluxes of 20.3 and 40.7 kg $s^{-1}m^{-2}$, with the properties of the fluid set to those of R-134a at a saturation temperature of 12.78 °C. The axial outlets were set as pressure outlets with a total gauge pressure of 0 Pa while the operating pressure was set to 454 kPa.

The simulation was run with the Reynolds stress model enabled. Initially run with 2000 iterations at steady-state, the simulation was then switched over to transient. The transient simulation was run using adaptive time-stepping to match the required residuals of 1e-4 for a simulation time of 2 min, though no changes beyond the development of the flow field were observed after the first 20 s.

5.2. Vapor simulation results

The vapor flow patterns within the bundle were found to default to two modes, depending on the method of initialization of the steady-state simulation. The first was as in Fig. 6 [both (a) and (b)], where one planar jet emerging from between the tubes immediately attaches to the headspace wall while the other two jets immediately merge. Near the top of the headspace, the merged jet combines with the jet attached to the wall. In the other mode observed, all three planar jets emerging from the tubes immediately merged and attached to a wall. Both modes were stable, albeit with small fluctuations, even after several minutes of simulated time. The same two flow patterns were observed at both mass fluxes, albeit with different velocities. The first mode was used for droplet simulation as it was closest to uniform headspace flow as could be achieved.

The highest velocities observed in Fig. 6 occurred at the holes in the distribution plate, reaching velocities of 9.74 m s^{-1} for the higher mass flux and 4.87 m s^{-1} for the lower mass flux. These velocities were approximately five times higher than the highest velocities observed between the tubes. Large recirculation regions were noted for both mass fluxes within the headspace, seen as the negative velocities (darker colors) on the upper left side of the headspace in Fig. 6(b). The jets in the headspace exceed 0.5 m s^{-1} from 30 mm above the tubes all the way to the distribution plate, two times higher than the velocity of 0.26 m s^{-1} if flow were uniform. Small perturbations were observed in the axial direction but flow was largely steady.

5.3. Droplet simulation setup

Use of a discrete-phase method for simulating droplet injection requires discretizing a particle mass flow both in velocity and size. For this simulation, a 9 by 9 grid of 81 uniform points 10 mm above the top of the tubes was chosen as the injection site. From each of these points, droplet parcels representing a number (or fraction) of droplets was released, having a specified diameter, velocity, and mass-flow rate, with the number or fraction of droplets per parcel calculated from the mass-flow rate, diameter, and time step. So, with the choice of 50 bins of diameters per 10 velocities, and 81 injection points, 40,500 parcels were injected into the simulation at each time step, with 500 discrete mass-flow rates. The number of diameter bins was chosen to roughly match the size of bins used in the experimental data acquisition. The velocity bin number was chosen to give a reasonable distribution based on measured velocities. In essence, the mass-flow rate of each velocity-diameter combination can be given by Eq. (5).

$$\dot{m}_{v,d} = \dot{m}_T \left(Y_{v,high} - Y_{v,low}\right)\left(Y_{d,low} - Y_{d,high}\right) \quad (5)$$

Table 5
Injection settings for 40.7 kg $s^{-1}m^{-2}$, $\dot{m}_T$=0.13 kg s^{-1}, 12.8 °C.

Velocity per bin (m s^{-1})			Mass			Diameter distribution ($N = 50$)			
Min	Max	Mean (simulation setting)	Cumulative fraction (Y_v)	Fraction ($Y_{v,high} - Y_{v,low}$)	Flow rate ($\dot{m}_v$, kg s^{-1})	d_{min}	$\bar{d}$	d_{max}	n
0.000	0.198	0.099	7.26E-01	7.26E-01	9.43E-02	1.286E-04	2.00E-03	2.76E-03	3.568
0.198	0.395	0.296	9.19E-01	1.94E-01	2.52E-02	1.286E-04	1.54E-03	2.04E-03	3.568
0.395	0.593	0.494	9.75E-01	5.56E-02	7.22E-03	1.286E-04	1.31E-03	1.69E-03	3.568
0.593	0.790	0.691	9.83E-01	8.64E-03	1.12E-03	1.286E-04	1.16E-03	1.47E-03	3.568
0.790	0.987	0.889	9.89E-01	5.23E-03	6.80E-04	1.286E-04	1.05E-03	1.31E-03	3.568
0.987	1.185	1.086	9.92E-01	3.66E-03	4.76E-04	1.286E-04	9.63E-04	1.19E-03	3.568
1.185	1.382	1.284	9.95E-01	2.72E-03	3.54E-04	1.286E-04	8.94E-04	1.10E-03	3.568
1.382	1.580	1.481	9.97E-01	2.11E-03	2.74E-04	1.286E-04	8.37E-04	1.02E-03	3.568
1.580	1.777	1.679	9.99E-01	1.67E-03	2.17E-04	1.286E-04	7.88E-04	9.47E-04	3.568
1.777	1.975	1.876	1.000E+00	1.35E-03	1.76E-04	1.286E-04	7.46E-04	8.89E-04	3.568

The variable $\dot{m}_T$ is the total mass flow of all liquid droplets into the simulation, Y_v is the cumulative mass fraction as a function of velocity, Y_d is the cumulative mass fraction as a function of diameter, and subscripts low and high denote the bounds of each bin by diameter or velocity.

The simulation software used allowed for automated discretization of the size distribution. However, discrete velocities had to be set by the user, meaning the parameters of the size distribution had to be set for each chosen velocity. For this simulation, 10 discrete velocities were used and placed at the mean velocity of each bin. The simulation software method for discretizing by size employed the Rosin-Rammler distribution equation, given in Eq. (6).

$$Y_d = e^{-\left(d/\bar{d}\right)^n} \tag{6}$$

The variable Y_d is the mass fraction of droplets greater than d, e is Euler's number, d is diameter, $\bar{d}$ is the mean diameter, and n is the spread parameter. The parameters of $\dot{m}_v$, d_{min}, d_{max}, and n had to also be set in the software to make use of the automatic discretization. The parameters d_{min} and d_{max} represent the minimum and maximum diameters of a distribution while N represents the total number of uniform-by-diameter bins. Together they definie the bounds of the size distribution as well as bin sizes. The mass-flow rate per velocity, $\dot{m}_v$, could also be described by

$$\dot{m}_v = \dot{m}_T\left(Y_{v,high} - Y_{v,low}\right) \tag{7}$$

meaning the mass flow per velocity is calculated based on the total mass flow of liquid and the mass fraction. Altogether, the preceding values define a discrete particle injection. The values used to simulate droplet flow for the 40.7 kg $s^{-1}m^{-2}$ mass flux at 12.8 °C are shown in Table 5.

With the exception of $\dot{m}_T$, total mass flow of liquid injected, settings of the discrete-phase simulation come from an analysis of the experimental results previously discussed. As discussed in the results section, $\dot{m}_T$ currently must be found by trial and error.

Experimental results for dryout conditions for both mass fluxes, saturation temperatures, and the highest heat flux were analyzed to determine droplet size and velocity distributions. Dryout conditions were chosen as this is the liquid level at which a pure vapor leaving the tubes is closest to reality. Droplets with a height above the bundle from 5 to 15 mm were binned by velocity and a least-squares fit to the Rosin-Rammler distribution was found per velocity bin. As the simulation involves the injection of particles, only particles with a zero or positive vertical velocity were used for analysis. Results of the analysis are shown in Fig. 7 as well as least-squares curve fits. The velocity axis denotes the maximum velocity of each bin.

Note that d_{min} is a constant (largely constrained by the minimum resolution of the camera and lens) and that n is chosen to be as well (note that n is displayed on the secondary axis on the right). The data for n are randomly distributed at about a value of 3.568. The experimental data for d_{max} and d_{mean} are fit well by a power fit with an offset.

A curve fit to correlate the cumulative mass fraction with velocity was also found using least squares, the equations for which are given in Fig. 8.

One curve fit is used to represent the data up to a velocity of 0.7 m s^{-1}, where all experimental data converge on a cumulative mass fraction of 0.98. From a velocity of 0.7 m s^{-1} to v_{max}, a separate curve applies. The term v_{max} denotes the maximum vapor velocity expected for full vapor flow between the tubes and was found from the vapor simulation previously described. The values of v_{max} are given in Table 3.

To complete the simulation, the droplets were given the density of saturated liquid R-134a corresponding to a temperature of 12.8 °C. The walls of the test section below the distribution plate, as well as the tubes, were set to have an "escape" boundary condition for the discrete phase, meaning any droplet that touched the walls was removed from the simulation. The walls above the distribution plate were set to a "reflect" boundary conditions, ensuring any droplets above the distribution plate left through the simulation's outlets.

The simulation was run with 12 iterations per time step of 0.01 s, resulting in scaled residuals below 1e-03. The rates of mass escaping through the tubes, walls, and outlets were monitored to determine when the headspace had reached a steady-state saturation. The simulation was then run an additional three times the length of time required to reach this saturation.

5.4. Droplet simulation results

A 10 mm slice showing the instantaneous droplet parcel distribution is shown in Fig. 9. The slice is centered on one set of the distribution plate holes. Larger droplets are restricted to the lower portion of the headspace while smaller droplets fill the entirety of the headspace and escape through the distribution plate. Medium sized droplets reach higher on the right side of the simulation than on the left side, corresponding with the recirculation and jetting seen in the vapor simulation in Fig. 6(b)

The distribution of liquid volume fractions was used to compare the experimental and simulation results. A trial-and-error method was used to determine the total mass-flow rate to be injected such that results matched the experimental results. Figs. 10 and 11 show the comparisons of liquid volume fractions for 12.8 °C at both 20.3 and 40.7 kg s^{-1} m^{-2} for several different simulated mass-flow rates of liquid.

For the mass flux of 20.3 kg m s^{-1}, the best match above approximately 30 mm is given by a total liquid-mass-flow injection of 0.012 kg s^{-1}, overestimating the volume fraction until both the experimental and all simulation volume fractions go to zero at

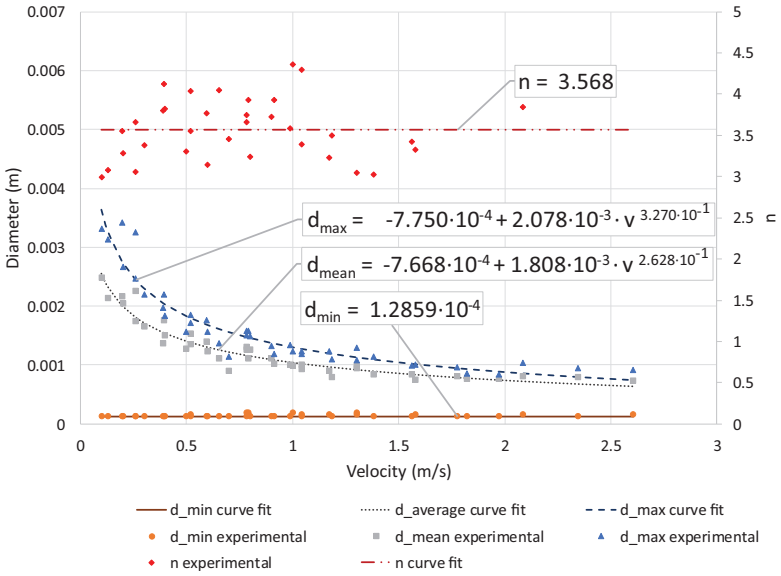

Fig. 7. Experimental and curve-fit parameters of Rosin-Rammler distribution by velocity.

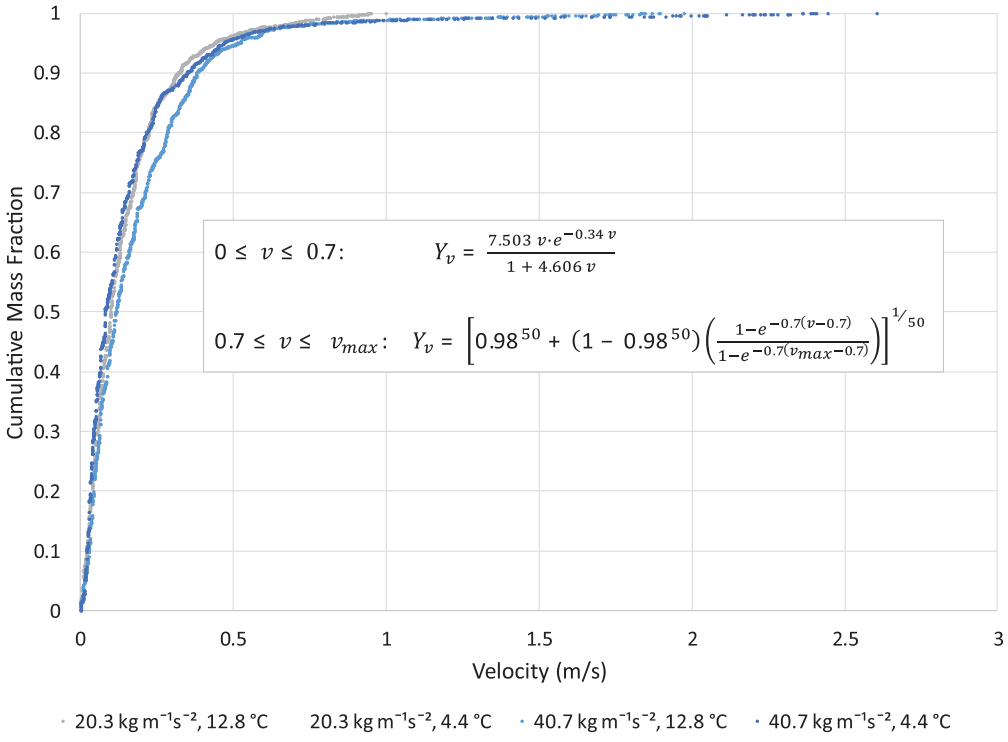

Fig. 8. Cumulative mass fraction as a function of maximum bin velocity.

approximately 57 mm above the tubes. With the exception of the first sample point at 17 mm, a total liquid-mass-flow injection of 0.015 kg s^{-1} provides a better match below 30 mm. For the higher mass flux of 40.7 kg s^{-1}, the best match above approximately 45 mm is given by a total liquid-mass-flow injection of 0.013 kg s^{-1} of the simulations tested, though at the highest point sampled all injections tested had approximately the same deviation from experimental results. Below 45 mm, results are mixed as to which injection flow rate matches best.

Interestingly, an initially non-intuitive result is that the mass-flow rate of the liquid injected can be much greater than the total vapor and liquid flow being simulated. This can be explained, however, by the differences between the simulation and physical system. In the physical system, droplets that would hit the walls largely collect into a film that flows down the wall back to the tubes, with the liquid being re-entrained. In the simulation, droplets that contact most walls disappear, negating the extra processing needed to handle collision, merging, and droplet breakup. As the intent is to explore both the liquid distribution and how much liquid escapes through the normal path of the distribution plate, the additional mass flow rate is acceptable.

6. Summary and discussion

Two dominant mechanisms thought to generate liquid droplets are vapor shear and surface-tension-dominated wave action. Based

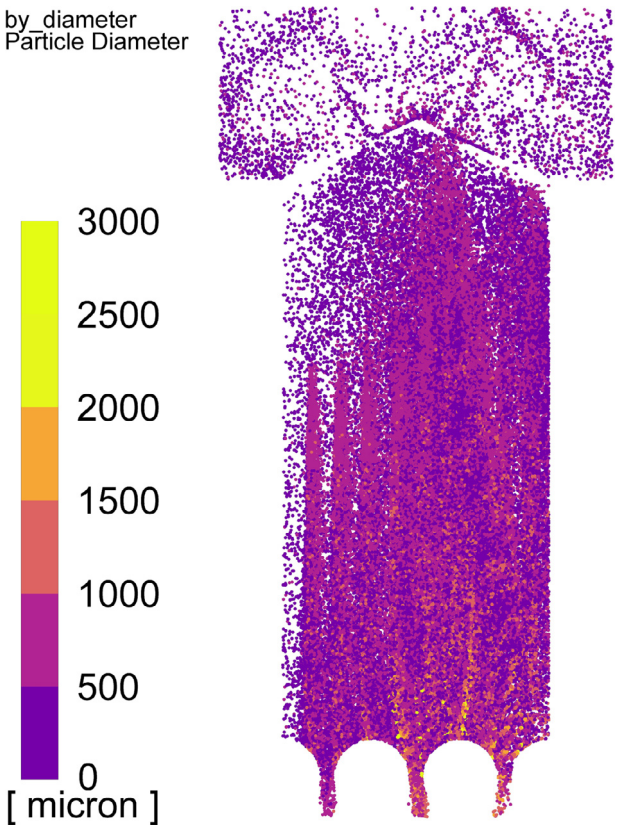

Fig. 9. Droplet parcel distribution in 10 mm slice, 40.7 kg $s^{-1}m^{-2}$, 12.8 °C.

on experimental results, as well as velocity-dependent correlations devised to implement the numerical simulation, shear is likely the dominant mechanism given the vapor velocities involved. However, as seen in the deviation from baseline in the liquid volume fraction of the flooded case in Fig. 4, higher liquid levels result in an increase of wave-generated droplets.

Two major flow regions within the headspace are identified based on expected vapor velocities. First, the maximum velocity occurs at the start of the headspace between the tubes, with velocities as shown in Table 3. The second regime occurs further up in the headspace. Contrary to the original expectation of slower uniform flow, numerical simulations, as in Fig. 6, show a very active region containing recirculation regions and relatively fast upward jets with velocities more than two times what would be expected with uniform flow.

The disparity in velocities allows the headspace to act as a separation chamber, the effectiveness of which is dependent on flow conditions and physical arrangement. For most of the conditions tested and presented, no appreciable liquid reaches the top of the headspace. However, the combination of certain conditions (flooded, high mass flux, high saturation temperature, high heat flux) can lead to droplets reaching the top of the headspace. As shown in Fig. 6, a region exists at the top of the headspace where the holes in the distribution plate accelerate the flow. Droplets that reach this region may be entrained in this higher vapor flow and be carried out. As discussed in Asher and Eckels (2018b), albeit described for R-123, velocity plays a key role in determining the maximum-sized droplet that vapor flow can lift.

The bundle used in both the experimental and numerical experiments had a constant-area, fixed-height headspace. As such, while flow may have continued to even out and decrease with increasing

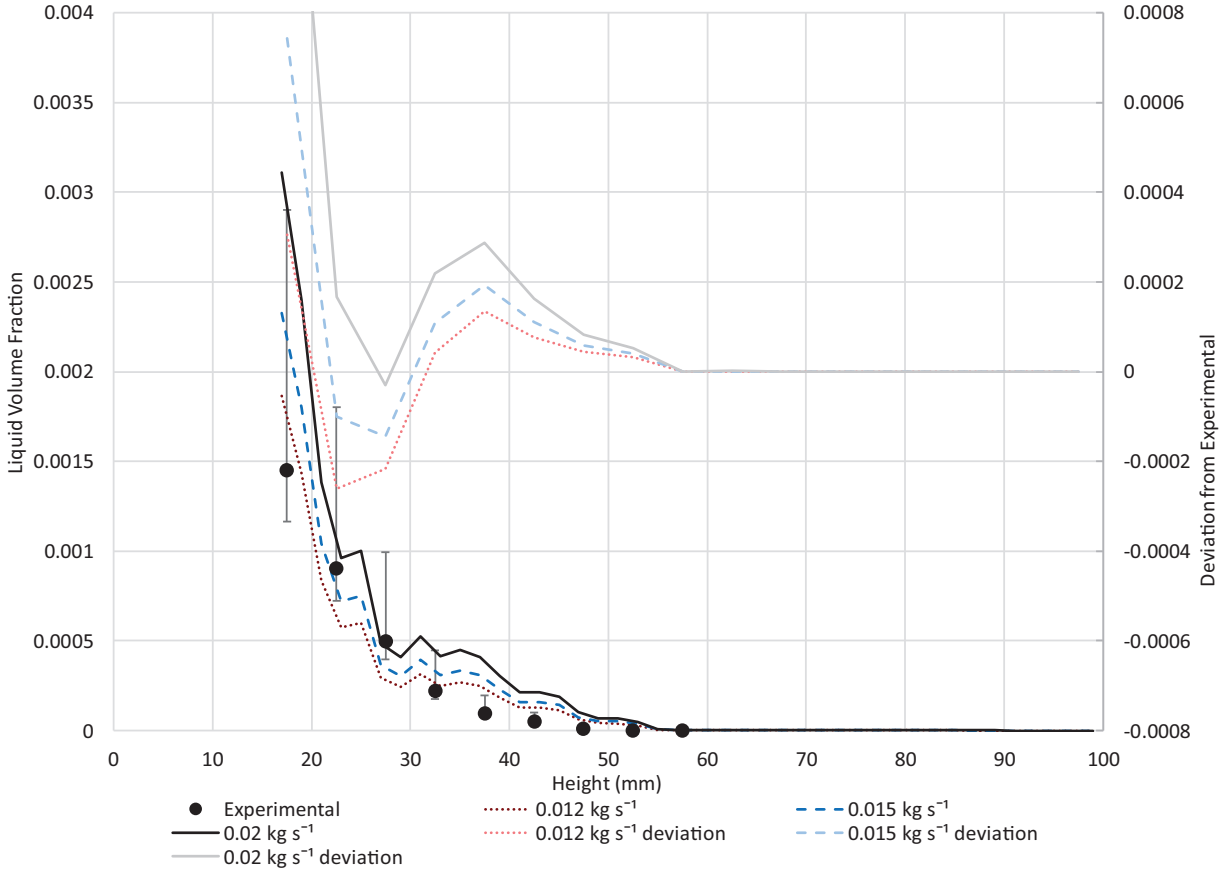

Fig. 10. Experimental vs. simulation liquid volume fraction, 12.8 °C, 20.3 kg m s^{-1}.

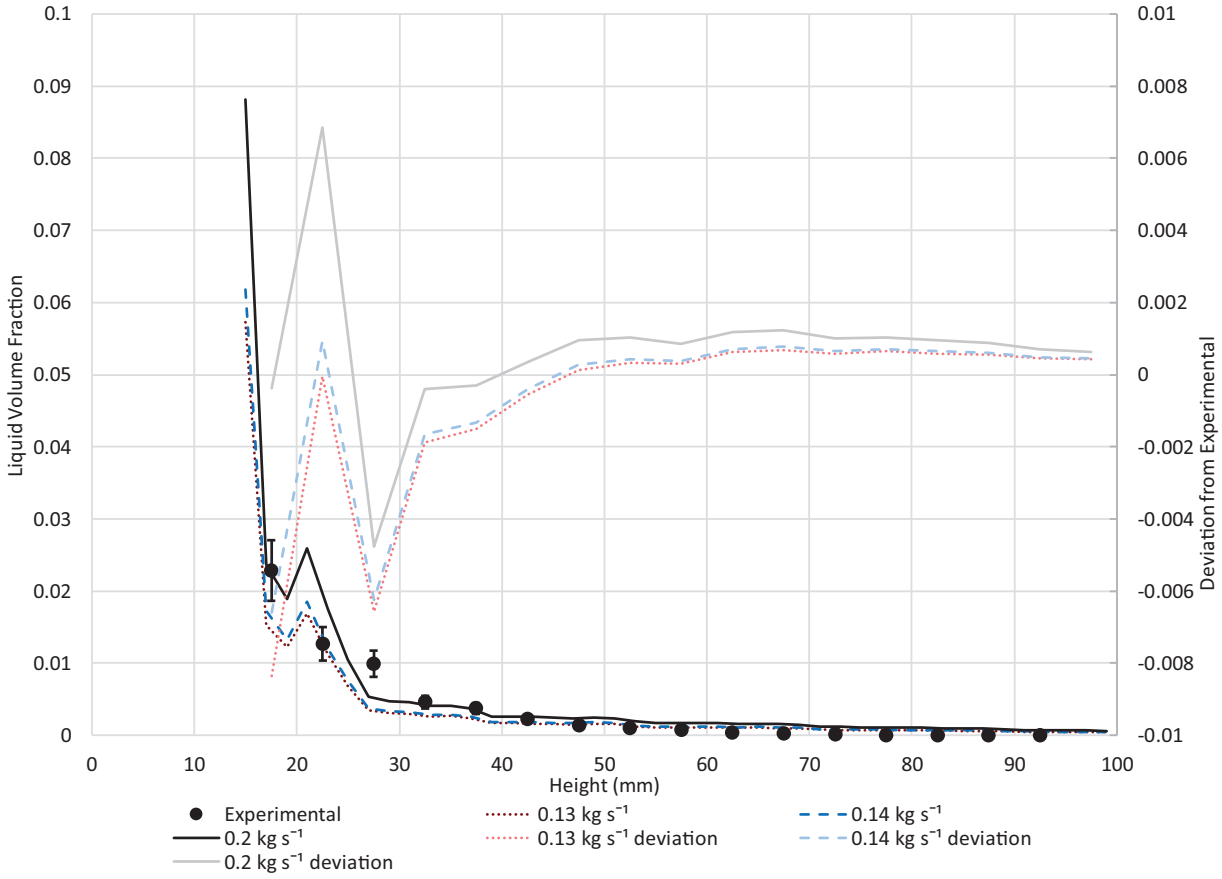

Fig. 11. Experimental vs. simulation liquid volume fraction, 12.8 °C, 40.7 kg m s^{-1}.

height, a minimum droplet size still exists that could be carried up to the top. An expansion of the walls would decrease velocities even further, improving the ability to separate droplets from the flow. While the distribution plate does contain velocity-increasing (and possibly carryover-increasing) holes, simulated droplets did impact on its surface, indicating its role in preventing carryover could be explored further. The numerical method presented shows promise for assisting in the design of an evaporator headspace. So far it has only been correlated for changes in velocity (through mass flux and saturation temperature), but an expansion of correlations involving liquid level and bundle arrangement would complement this work. Components and parameters such as the distribution plate, tube-gap sizes, and liquid-level settings could all be varied with the simulation to define an optimal design.

7. Conclusion

The headspace of a flooded evaporator is a complex environment. These spaces typically act as separation vessels that prevent or reduce harmful liquid droplets from reaching the compressor. A system was built to characterize the droplet distribution in the headspace above a tube-bundle evaporator for refrigerant R-134a. A camera system and dual-pulsed Nd:YAG laser in a shadowgraphy arrangement was used to capture multitudes of images of the headspace, and software was used to process and match droplets from the images.

System conditions were varied such that the evaporator experienced mass fluxes of 20.3 and 40.7 kg $s^{-1}m^{-2}$, top-rows heat fluxes from 15.8 and 31.5 kWm^{-2}, and outlet saturation temperatures of 4.4 and 12.8 °C. Levels of the liquid in the evaporator were varied such that the top rows went from flooded to dryout.

Results were presented and discussed. Liquid distribution in the headspace was found to be a strong function of all varied properties, particularly liquid level, mass flux, and saturation temperature. The results were complemented with a numerical simulation based on Lagrangian physics implemented in a discrete-phase model with its settings based on correlations devised from the experimental data for dryout conditions. Good correlation was found between the liquid volume fractions of the experimental and numerical results. This simulation method can be used to develop physical dimensions and shape of the headspace area. Future work will include an expansion of correlations of droplet velocities and diameters to include variations in liquid level, refrigerants, and heat flux.

Acknowledgements

The research behind this work was funded through ASHRAE RP-1556 (Asher and Eckels, 2018a).

References

Ahmadpour, A., Noori Rahim Abadi, S.M.A., Meyer, J.P., 2018. Numerical investigation of pool boiling on a staggered tube bundle for different working fluids. Int. J. Multiph. Flow 104, 89–102.
Asher, W., Eckels, S., 2018a. RP-1556 – Characterization of liquid refrigerant flow emerging from a flooded evaporator tube bundle. ASHRAE, Atlanta, GA.
Asher, W., Eckels, S.J., 2018b. Characterization of liquid refrigerant R-123 flow emerging from a flooded evaporator tube bundle. Sci. Tech. Built Environ. 1–13.
Blaisot, J.B., Yon, J., 2005. Droplet size and morphology characterization for dense sprays by image processing: application to the diesel spray. Exp. Fluids 39, 977–994.
Cheng, L., Ribatski, G., Thome, J.R., 2008. Two-phase flow patterns and flow-pattern maps: fundamentals and applications. Appl. Mech. Rev. 61, 0508021–05080228.

Dai, Z., Chou, W.H., Faeth, G.M., 1998. Drop formation due to turbulent primary breakup at the free surface of plane liquid wall jets. Phys. Fluids 10, 1147–1157.
Gorgy, E., Eckels, S., 2013. Convective boiling of R-134a and R-123 on an enhanced tube bundle with standard pitch, RP-1316. HVAC&R Res 19, 193–206.
Gorgy, E., Eckels, S., 2016. Convective boiling of R-134a on enhanced-tube bundles. Int. J. Refrigeration 68, 145–160.
Gorgy, E., Eckels, S., 2019. Convective boiling of R-123 on enhanced-tube bundles. Int. J. Heat Mass Transf.
Grant, I.D.R., Chisholm, D., 1979. Two-phase flow on the shell-side of a segmentally baffled shell-and-tube heat exchanger. J. Heat Transf. Trans. ASME 101, 38–42.
Gupta, A., 2005. Enhancement of boiling heat transfer in a 5×3 tube bundle. Int. J. Heat Mass Transf. 48, 3763–3772.
Hay, K.J., Liu, Z.C., Hanratty, T.J., 1998. A backlighted imaging technique for particle size measurements in two-phase flows. Exp. Fluids 25, 226–232.
Jung, D., Kim, Y., Ko, Y., Song, K., 2003. Nucleate boiling heat transfer coefficients of pure halogenated refrigerants. Int. J. Refrigeration 26, 240–248.
Kang, M.-G., 2016. Pool boiling heat transfer from an inclined tube bundle. Int. J. Heat Mass Transf. 101, 445–451.
Kanizawa, F.T., Ribatski, G., 2016. Two-phase flow patterns across triangular tube bundles for air-water upward flow. Int. J. Multiph. Flow 80, 43–56.
Kashdan, J.T., Shrimpton, J.S., Whybrew, A., 2003. Two-phase flow characterization by automated digital image analysis. Part 1: fundamental principles and calibration of the technique. Part. Part. Syst. Charact. 20, 387–397.
Kashdan, J.T., Shrimpton, J.S., Whybrew, A., 2004. Two-Phase flow characterization by automated digital image Analysis. Part 2: application of PDIA for sizing sprays. Part. Part. Syst. Charact. 21, 15–23.
Kondo, M., Nakajima, K.-i., 1980. Experimental investigation of air-water two phase upflow across horizontal tube bundles - 1. flow pattern and void fraction. Bull. JSME 23, 385–393.
Li, P., Eckels, S.J., Mann, G.W., Zhang, N., 2018. A method of measuring turbulent flow structures with particle image velocimetry and incorporating into boundary conditions of large eddy simulations. J. Fluids Eng. 140, 071401–071411 071401-.
Minocha, N., Joshi, J.B., Nayak, A.K., Vijayan, P.K., 2016. 3D CFD simulation of passive decay heat removal system under boiling conditions: role of bubble sliding motion on inclined heated tubes. Chem. Eng. Sci. 145, 245–265.
Patruno, L.E., Marchioro Ystad, P.A., Marchetti, J.M., Dorao, C.A., Svendsen, H.F., Jakobsen, H.A., 2010. Liquid entrainment from a wetted wire exposed to a high gas flow rate in cross flow. Chem. Eng. Sci. 65, 6397–6406.
Ribatski, G., Saiz Jabardo, J.M., da Silva, E.F., 2008. Modeling and experimental study of nucleate boiling on a vertical array of horizontal plain tubes. Exp. Therm. Fluid Sci. 32, 1530–1537.
Robinson, D.M., Thome, J.R., 2004. Local bundle boiling heat transfer coefficients on a turbo-BII HP tube bundle (RP-1089). HVACR Res. 10, 441–457.
Schlup, J., Eckels, S., 2017. Two phase flow visualization in evaporator tube bundles using experimental and numerical techniques. In: Proceedings of the 2nd Thermal and Fluids Engineering Conference and 4th International Workshop on Heat Transfer. Las Vegas. ASFTE.
Ulbrich, R., Mewes, D., 1994. Vertical, upward gas-liquid two-phase flow across a tube bundle. Int. J. Multiph. Flow 20, 249–272.
van Rooyen, E., Agostini, F., Borhani, N., Thome, J.R., 2012. Boiling on a tube bundle: part i –Flow visualization and onset of dryout. Heat Transf. Eng. 33, 913–929.
Van Rooyen, E., Thome, J.R., 2013. Pressure drop data and prediction method for enhanced external boiling tube bundles with R-134a and R-236fa. Int. J. Refrigeration 36, 1669–1680.
Van Rooyen, E., Thome, J.R., 2014. Flow boiling data and prediction method for enhanced boiling tubes and tube bundles with R-134a and R-236fa including a comparison with falling film evaporation. Int. J. Refrigeration 41, 60–71.